INTERNATIONAL JOURNAL OF
NUMERICAL ANALYSIS AND MODELING
Volume 12, Number 3, Pages 430–454

VARIATIONAL MULTISCALE A POSTERIORI ERROR ESTIMATION FOR 2^{nd} AND 4^{th}-ORDER ODES

DIEGO IRISARRI AND GUILLERMO HAUKE

Abstract. In this paper, an explicit a posteriori error estimator is developed for second and fourth order ODEs solved with the Galerkin method that, remarkably, provides exact pointwise error estimates. The error estimator is derived from the variational multiscale theory, in which the subgrid scales are approximated making use of fine-scale Green's functions. This methodology can be extended to any element type and order. Second and fourth order differential equations cover a great variety of problems in mechanics. Two examples with application in elasticity have been studied: the axially loaded beam and the Euler-Bernoulli beam. Because the error estimator is explicit, it can be very easily implemented and its computational cost is very small. Apart from pointwise error estimates, we present local and global a posteriori error estimates in the L^1-norm, the L^2-norm and the H^1-seminorm. Finally, convergence rates of the error and the efficiencies of the estimator are analyzed.

Key words. a posteriori error estimation, 1D linear elasticity, Euler-Bernoulli beam, pointwise error, variational multiscale theory.

1. Introduction

Second and 4^{th}-order ODEs and, in general, elliptic differential equations have been thoroughly studied using finite element methods (FEM). Specially, the standard Galerkin method gives rise to satisfactory solutions for these types of equations, helping the FEM achieve a widespread use by scientist and engineers. However, it is well-known that numerical methods have an inherent error that, basically, depends on the discretization and the order of the numerical method. Accordingly, in order to evaluate the quality of the FEM solution, it is convenient to quantify the numerical error which is committed. Furthermore, a posteriori error estimation can be exploited by adaptive methods to reduce the error where it is more beneficial.

There exists a broad literature on a posteriori error estimation for FEM which can be classified in three groups [2]:

(1) *Residual-based methods.* The proposed estimator belongs to this category. They are also called *explicit methods* since the error estimate is based only on the information provided by the FEM solution. The error is computed via interior residuals or/and inter-element residuals. They were proposed for the first time by Babuška et al. [4, 5].
(2) *Recovery-based methods.* Zienkiewicz and Zhu [38] developed these techniques, which take advantage of superconvergent properties of the solution. Satisfactory results are achieved for a wide variety of problems. The main idea consists of estimating the error by comparing a smoothed gradient with the gradient of the FEM solution. A general background might be found in [1].

Received by the editors February 28, 2014 and, in revised form, March 22, 2014.
2000 *Mathematics Subject Classification.* 35R35, 49J40, 60G40.
This research was supported by Spanish MECD under FPU grant (AP210-2073), the Ministerio de Ciencia e Innovación under contract MTM2010-20463, Gobierno de Aragón and FEDER funding from the European Union.

(3) *Auxiliary-problem-based methods.* Lately, important advances have been made in this category in which the error is estimated by solving new differential equations. For this reason, they also receive the name of *implicit methods*. They involve the calculation of residuals of the FEM solution. Typically, these differential equations are applied to a subdomain (an element or a patch of elements). Many researchers have worked in this matter [6, 3]. Ladèveze et al. proposed a local error estimator based on the recovery of equilibrated fluxes [28, 29]. Applications to linear elasticity have been made recently by Verfürth et al. [31], Carstensen et al. [8], Parés, Díez, Huerta and co-workers [35, 9] and Masud et al. [32], where nearly incompressible elasticity is studied. Goal-oriented error estimators have been developed, see Oden et al. [34, 37], in which the dual problem is solved and it involves the computation of influence functions in order to relate the residuals to specific quantities of interest.

In this work, the error estimator is based on the variational multiscale theory (VMS) [24, 26], in which the solution is split into resolved and unresolved scales. Precisely, the unresolved scales present a paradigm from which the error of the finite element solution can be calculated or estimated. In the theory, the interior residuals and inter-element jumps emerge naturally as error sources.

Previous works of the group on this technology were devoted to the transport equation solved with stabilized methods [18, 19, 21, 17, 20, 15, 22]. Here, this technology is extended to second and fourth order differential equations which can be solved with the Galerkin method. Furthermore, following [27] the fine-scale Green's functions have been numerically computed and exploited to obtain expressions for the local and global errors. This procedure has been clarified in the Appendix, so it can be extended to other equations and any element type.

Following the variational multiscale theory, a few relevant articles have studied the fine scales, or unresolved scales, [11, 10, 27, 30], revealing that under most circumstances they are nearly local. That is, for certain class of methods the error is mostly confined inside the element. This is an important property that has been exploited in this work to calculate the error in each element.

Also, beyond existing work on VMS error estimation, pointwise error estimates are studied in this paper. This field has been treated previously for other authors in elliptic problems such as Nochetto [33] using regularized Green's functions. A prominent work was carried out by Prudhomme et al. [36] where quantities of interest of the error are measured and tested in one-dimensional problems. However, the present theory provides a simple way to attain an exact representation of the pointwise error.

Following the introduction, we present in Sec. 2 the background of *VMS error estimation*. The split of coarse and fine-scale spaces is discussed and it is shown that the error can be assessed using the fine-scale variational form. At the end of the section, the general expressions for the pointwise error estimator and for a domain are established. In Sec. 3 and 4, we address the error estimation for the 1-D axially loaded beam and the Euler-Bernoulli beam problem, respectively. In both sections, numerical examples illustrate the behavior of the error estimator. In Section 5, we explain how this estimator can be extended to multi-dimensional problems. Finally, we remark the conclusions of this work.

2. The VMS error estimation framework

2.1. FEM formulation.

2.1.1. Strong form. Let Ω be a bounded domain in $\mathbb{R}$ with boundary Γ, which can be divided into two parts, Γ_g and Γ_h, such that $\Gamma_g \cup \Gamma_h = \Gamma$ and $\Gamma_g \cap \Gamma_h = \emptyset$. The essential boundary condition, g, is applied on Γ_g and the natural boundary condition, h, on Γ_h.

The strong form, which stems from the equilibrium equations, consists of finding $u \in \mathcal{S} : \Omega \to \mathbb{R}$, such that for the given functions $f : \Omega \to \mathbb{R}$, $g : \Gamma_g \to \mathbb{R}$ and $h : \Gamma_h \to \mathbb{R}$, the following equations are satisfied:

$$\left\{ \begin{array}{rcll} \mathcal{L}u & = f & \text{in} & \Omega \\ u & = g & \text{on} & \Gamma_g \\ \mathcal{B}u & = h & \text{on} & \Gamma_h \end{array} \right. \tag{1}$$

where $\mathcal{L}$ is a generic differential operator and $\mathcal{B}$ an operator acting on Γ_h.

2.1.2. Weak form. The weak form is obtained by multiplying the strong form equation by weighting functions. Both the trial solution and the weighting functions must belong to suitable spaces. Therefore, let $w \in \left\{ \mathcal{V} \subset (H^r(\Omega)) : w|_{\Gamma_g} = 0 \right\}$ be the weighting functions and let $u \in \left\{ \mathcal{S} \subset (H^r(\Omega)), u|_{\Gamma_g} = g \right\}$ be the trial solution with r denoting the order of the spaces. In our case, we adopt $r = 1$ for the beam problem with an axial force (2^{nd}-order ODE) and $r = 2$ for the Euler-Bernoulli beam problem (4^{th}-order ODE).

Accordingly, we can establish the variational form as: Find $u \in \mathcal{S}$ such that

$$a(w, u) = (w, f) + (w, h)_{\Gamma_h} \qquad \forall w \in \mathcal{V} \tag{2}$$

where $a(\cdot, \cdot)$ is the bilinear form, $(\cdot, \cdot)$ the $L^2(\Omega)$ inner product and $(\cdot, \cdot)_{\Gamma_h}$ the $L^2(\Gamma_h)$ inner product on Γ_h. For each particular problem, we will expand these operators later.

So as to introduce the FEM method, the domain, Ω, must be discretized into n_{el} non-overlapping elements with domain Ω^e. We define $\widetilde{\Omega}$ as the union of element interiors, $\widetilde{\Omega} = \bigcup_{e=1}^{n_{\text{el}}} \Omega^e$.

We establish the finite spaces $\mathcal{S}^h \subset \mathcal{S}$ and $\mathcal{V}^h \subset \mathcal{V}$ for the trial FEM solution and the weighting functions, respectively,

$$\begin{array}{l} \mathcal{S}^h = \{u_h \in (H^r(\Omega)) \ \mid \ u_{h|\Omega^e} \in \mathbb{P}_k, u_{h|\Gamma_g} = g, \forall \Omega^e \in \widetilde{\Omega}\} \\ \mathcal{V}^h = \{w_h \in (H^r(\Omega)) \ \mid \ w_{h|\Omega^e} \in \mathbb{P}_k, w_{h|\Gamma_g} = 0, \forall \Omega^e \in \widetilde{\Omega}\} \end{array} \tag{3}$$

where $\mathbb{P}_k$ denotes the space of polynomials of degree k. Thus, the standard Galerkin method reads:

Find $u_h \in \mathcal{S}^h$ such that

$$a(w_h, u_h) = (w_h, f) + (w_h, h)_{\Gamma_h} \qquad \forall w_h \in \mathcal{V}^h \tag{4}$$

2.2. Variational multiscale theory. The variational multiscale method was rigorously developed in [24, 26]. It consists of splitting the weak solution and the weighting functions into coarse scales (or resolved scales) and fines scales (or unresolved scales),

$$\begin{array}{lll} u & = \bar{u} + u' & \bar{u} \in \bar{\mathcal{S}}, \quad u' \in \mathcal{S}' \\ w & = \bar{w} + w' & \bar{w} \in \bar{\mathcal{S}}, \quad w' \in \mathcal{S}' \end{array}$$

We can identify the coarse scales with the selected finite element spaces, $\mathcal{S}^h$ and $\mathcal{V}^h$. On the other hand, the fine scales represent the unresolved scales, which are defined in an infinite-dimensional space, such that $\mathcal{S} = \bar{\mathcal{S}} \oplus \mathcal{S}'$ and $\mathcal{V} = \bar{\mathcal{V}} \oplus \mathcal{V}'$ for the trial functions and the weighting functions, respectively. Thus, in what follows, u' can be identified with the finite element error.

If the multiscale concept is introduced in Eq. (4), the variational formulation can be transformed into

$$a(\bar{w},\bar{u}) + a(\bar{w},u') = (\bar{w},f) + (\bar{w},h)_{\Gamma_h} \qquad \forall \bar{w} \in \bar{\mathcal{S}} \tag{5a}$$

$$a(w',\bar{u}) + a(w',u') = (w',f) + (w',h)_{\Gamma_h} \qquad \forall w' \in \mathcal{S}' \tag{5b}$$

It may be observed that Eq. (5a) involves the coarse scales, whereas Eq. (5b) represents the fine scales, which play a relevant role in error estimation.

2.3. Error estimation and fine-scale Green's functions. In this section, the a posteriori error estimator based on the variational multiscale theory is described. It is shown that the interior residual is the only error source and a post-processing of the FEM solution is enough in order to calculate the committed error.

For this purpose, we make use of the Eq. (5b) and the fine-scale Green's function concept [24, 26, 27]. This technology has been applied to the transport equation in [18, 19, 21, 17, 20] with positive results.

Taking Eq. (5b), for nodally exact methods the error can be calculated from the following expression

$$a(w',u') \quad = (w', f - \mathcal{L}\bar{u}) + (w', h - \mathcal{B}\bar{u})_{\Gamma_h} \qquad \forall w' \in \mathcal{S}' \tag{6}$$

Assuming that the FEM solution satisfies exactly the Neumann boundary condition, it can be seen that the error depends only on the FEM solution residual, $f - \mathcal{L}\bar{u}$. At this point, the fine-scale Green's function is introduced and the error may be expressed by $u' = \mathcal{G}'(f - \mathcal{L}\bar{u})$, where $\mathcal{G}'$ is the fine-scale Green's operator. Hughes and Sangalli established a general expression for this operator in [27], namely

$$\mathcal{G}' = \mathcal{G} - \mathcal{G}\mathcal{P}^T(\mathcal{P}\mathcal{G}\mathcal{P}^T)^{-1}\mathcal{P}\mathcal{G} \tag{7}$$

where $\mathcal{G}$ is the classical Green's function operator which represents the inverse of the differential operator $\mathcal{L}^{-1}$. $\mathcal{P}$ is an orthogonal projector, $\mathcal{P} : \mathcal{S} \to \bar{\mathcal{S}}$ such that $\mathcal{P}v = \bar{v}$ and $\mathcal{P}v' = 0$.

The operator $\mathcal{G}$ and the projector $\mathcal{P}$ can be approximated by matrix operators $\mathbf{G}$ and $\mathbf{P}$, respectively. In order to compute them, the first stage is to set up a fine mesh and the associated basis functions ϕ_i. Operating with this basis we can obtain the matrix $\mathbf{G}$ that can be expressed as $\mathbf{G} = \mathbf{L^{-1}}$, where $L_{ij} = (\mathcal{L}\phi_j, \phi_i)$. This process is also explained in [27]. Therefore, (7) is transformed into

$$\mathbf{G}' = \mathbf{G} - \mathbf{G}\mathbf{P}^T(\mathbf{P}\mathbf{G}\mathbf{P}^T)^{-1}\mathbf{P}\mathbf{G} \tag{8}$$

The second step consists of selecting the appropriate projector to estimate the error of the standard Galerkin method. As it was said, the exact solution u is decomposed into the FEM solution (or coarse solution), $\bar{u}$, and the unresolved scales, u', which represent the numerical error. In our case, the projector that is proposed to estimate the error is the bilinear form $a(\cdot,\cdot)$, i.e., the Galerkin projector. Accordingly, the fine-scale Green's functions are orthogonal with respect to $a(\cdot,\cdot)$ for all $\bar{w}$ belonging to $\bar{\mathcal{S}}$. Therefore, it is accomplished that the error, u', belongs to the kernel of this projector, $\mathcal{P}u' = 0$, due to the Galerkin orthogonality property $a(u',\bar{w}) = 0\ \forall \bar{w} \in \bar{\mathcal{S}}$. In the appendix, the process to obtain the projection operator is explained.

In order to obtain numerically the Green's function matrices $\mathbf{G}$ and $\mathbf{G}'$, we have used a (0,1) domain with a uniform fine mesh, with an element size h_e^f and homogeneous Dirichlet boundary condition. The shape functions associated with this fine mesh are considered as an approximation of the space $\mathcal{S}$. Then, it is selected a coarse mesh with an element size h_e^c ($h_e^c >> h_e^f$). Similarly, the shape

functions associated with the coarse mesh are assumed to be the $\bar{\mathcal{S}}$ space. As a result, the projection operator is clearly defined $\mathbf{P} : \mathcal{S} \to \bar{\mathcal{S}}$.

The fine-scale Green's function $g'(x, y)$ is obtained by means of $g'(x, y) = \Sigma_{i,j} G'_{ij} \phi_j(x) \phi_i(y)$, where $\phi_j(x)$ and $\phi_i(y)$ are the basis functions of the fine mesh. It will be shown in the numerical examples that $g'(x, y)$ is a local function, i.e., it is negligible when x and y do not belong to the same element.

Once the fine-scale Green's function is obtained, we can estimate the error. If we recall Eq. (6), the error u' can be expressed as

$$u'(x) = \int_{\widetilde{\Omega}} g'(x, y)(f - \mathcal{L}\bar{u})(y) \, \mathrm{d}\Omega_y \tag{9}$$

It is assumed that the fine-scale Green's function, $g'(x, y)$, is local and the support of these functions are defined inside the element. Accordingly, the integral in Eq. (9) can be extended to the element domain, Ω^e,

$$u'(x) = \int_{\Omega^e} g'(x, y)(f - \mathcal{L}\bar{u})(y) \, \mathrm{d}\Omega_y \quad \text{in} \quad \Omega^e \tag{10}$$

2.3.1. Piecewise constant residuals. If the residual is piecewise constant, $(f - \mathcal{L}\bar{u})(y) \in \mathcal{P}_0$, the pointwise error expression is

$$u'(x) = (f - \mathcal{L}\bar{u}) \int_{\Omega^e} g'(x, y) \, \mathrm{d}\Omega_y \quad \text{in} \quad \Omega^e \tag{11}$$

Since $g'(x, y)$ is zero on the element boundary, residual-free bubble functions can be introduced. As we can see, this functions are related to the intrinsic scales concept [14, 19, 24, 15, 12, 13, 7], that is,

$$b_0^e(x) = \int_{\Omega^e} g'(x, y) \, \mathrm{d}\Omega_y \tag{12}$$

Obviously, the bubble function depends on the coarse mesh size, h_e. Taking a general norm at both sides of Eq. (11)

$$||u'(x)||_{Z(\Omega^e)} = ||b_0^e(x)||_{Z(\Omega^e)} \, |(f - \mathcal{L}\bar{u})| \tag{13}$$

where $||\cdot||_Z$ is a given norm. Z may refer to the L^1-norm, the L^2-norm or the H^1-seminorm. The intrinsic scales for error estimation, τ_Z^0, depend on the local mesh size and the bubble function,

$$\tau_Z^0 = \frac{||b_0^e(x)||_{Z(\Omega^e)}}{\mathrm{meas}(\Omega^e)^{1/r}} \tag{14}$$

Therefore, the elemental error estimator is expressed as

$$\boxed{||u'(x)||_{Z(\Omega^e)} = \mathrm{meas}(\Omega^e)^{1/r} \tau_Z^0 \, |(f - \mathcal{L}\bar{u})|} \tag{15}$$

2.3.2. Approximation for higher order residuals. When the residual is not piecewise constant, the residual may be decomposed in Taylor series and Eq. (10) can be expressed as

$$\boxed{u'(x) \quad = b_0(x)(f - \mathcal{L}\bar{u})(c_i) + \sum_{k=1}^{\infty} b_k^e(x) \frac{1}{k!} \frac{d^k (f - \mathcal{L}\bar{u})}{dy^k}\bigg|_{y=c_i}} \tag{16}$$

where c_i is the central point of the element and b_k^e is the k^{th}-order residual-free bubble, defined as

$$
\begin{aligned}
b_0^e(x) &= \int_{\Omega^e} g'(x,y)\mathrm{d}\Omega_y \\
b_1^e(x) &= \int_{\Omega^e} g'(x,y)(y-c_i)\mathrm{d}\Omega_y \\
b_2^e(x) &= \int_{\Omega^e} g'(x,y)(y-c_i)^2\mathrm{d}\Omega_y \\
&\dots \\
b_k^e(x) &= \int_{\Omega^e} g'(x,y)(y-c_i)^k\mathrm{d}\Omega_y
\end{aligned}
\tag{17}
$$

Eq. (16) is the general expression for the *pointwise error* and it will be particularised in each problem.

Now, we can define the error intrinsic time scales, τ_Z^k, which depend on the local mesh size and the bubble functions,

$$
\tau_{Z(\Omega^e)}^k = \frac{||b_k^e(x)||_{Z(\Omega^e)}}{\text{meas}(\Omega^e)^{1/r}} \tag{18}
$$

For the L^1-norm, r is equal to 1, and for the L^2-norm and the H^1-seminorm, r is 2. Introducing the error time scales, τ_Z^k, and taking a suitable norm we obtain an elemental error expression which can be exact when the residual is piecewise constant or an upper bound when the residual is of higher order,

$$
\boxed{
\begin{aligned}
||u'(x)||_{Z(\Omega^e)} \leq \quad & \text{meas}(\Omega^e)^{1/r}\tau_Z^0\,|(f-\mathcal{L}\bar{u})(c_i)| + \\
& \sum_{k=1}^{\infty} \text{meas}((\Omega^e)^{1/r}\tau_Z^k \frac{1}{k!}\left|\frac{d^k(f-\mathcal{L}\bar{u})}{dy^k}\right|_{y=c_i}\Bigg|
\end{aligned}
} \tag{19}
$$

2.4. Effectivity index. A way of evaluating the quality and accuracy of an error estimator consists of calculating the efficiency or effectivity index. The effectivity is defined as the ratio between the predicted error norm and the true error norm,

$$
I_{\text{eff}} = \frac{||\text{Predicted error}||}{||\text{True error}||} \tag{20}
$$

This concept can be applied both to the whole domain (obtaining a global effectivity), and to each element (obtaining a local effectivity). Hence, the local and global effectivities are expressed as

$$
\begin{aligned}
I_{\text{eff}}^e &= \frac{||\eta^e||_{\Omega^e}}{||u-\bar{u}||_{\Omega^e}} \qquad \text{(local effectivity)} \\
I_{\text{eff}}^G &= \frac{||\eta||_{\Omega}}{||u-\bar{u}||_{\Omega}} \qquad \text{(global effectivity)}
\end{aligned}
\tag{21}
$$

with η^e being the error estimation in an arbitrary element Ω^e and $||\cdot||_{\Omega^e}$ represents a norm.

Next, we evaluate the error estimator with several examples. The first benchmark consists of a beam with a sinusoidal load, f. The second problem is the Euler-Bernoulli beam problem, which is a 4^{th}-order ODE.

3. 1-D axially loaded beam

In Fig. 1, a beam is loaded with a sinusoidal axial force. The general strong form of the problem is

$$\begin{cases} EA\dfrac{d^2u}{dx^2} = -f & \text{in} \quad \Omega \\ u = g & \text{on} \quad \Gamma_g \\ EA\dfrac{du}{dx} = h & \text{on} \quad \Gamma_h \end{cases} \tag{22}$$

where E is the elastic modulus and A is the transversal section. The variable u is the unknown axial displacement. The Dirichlet boundary condition expresses the imposed displacement g on Γ_g and the Neumann boundary condition means the imposed stress h on Γ_h.

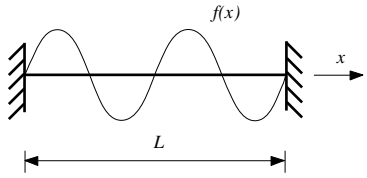

FIGURE 1. Beam with an axial force.

Particularly, it is seen in Fig. 1 that at both ends of the beam the displacement is zero. Finally, f is the axial force, which in our case is sinusoidal,

$$f = f_0 \sin(2^m \pi x) \tag{23}$$

with f_0 being an arbitrary constant and m a positive integer. For $L = 1$, the analytical solution can be obtained by integrating two times the strong formulation,

$$u = \frac{1}{4^m \pi^2 EA} f_0 \sin(2^m \pi x) \tag{24}$$

To construct the variational form, we define the weighting and trial function spaces. Let $w \in \left\{\mathcal{V} \subset (H^1(\Omega)) : w|_{\Gamma_g} = 0\right\}$ be the weighting functions and let $u \in \left\{\mathcal{S} \subset (H^1(\Omega)), u|_{\Gamma_g} = g\right\}$ be the trial functions. The weak form can be written as

$$a(w,u) = (w,f) \qquad \forall w \in \mathcal{V} \tag{25}$$

where

$$\begin{aligned} a(w,u) &= -\int_0^l w_{,x} EA u_{,x}\, \mathrm{d}x + wh|_{\Gamma_h} \\ (w,f) &= -\int_0^l wf\, \mathrm{d}x \end{aligned} \tag{26}$$

For the FEM formulation, we employ piecewise linear finite elements, $u_h \in \mathbb{P}_1$ and $w_h \in \mathbb{P}_1$, in a uniform partition of 2^n elements (n is an integer) with the characteristic that the node positions are at $x_k = k/2^n$ for $k = 0, 1, 2, 3, ..., 2^n$.

It is observed that u_h will be a linear interpolation of the exact solution. Therefore, if we take $m \geq n$, u_h is zero on the whole domain. The present example is inspired by the problem proposed by Ainsworth and Oden in [2], in which it is shown some downsides of recovery-based error estimators. For instance, in this problem with $m \geq n$, recovery-based error estimators predict a zero error whereas

the error is significant. In fact, the FEM error coincides with the exact solution, $u' = u - u_h = u$.

Therefore, since the FEM solution is nodally exact, the fine scale space $\mathcal{S}'$ is the space of bubble functions

$$\mathcal{S}' = \bigoplus_{e=1,\dots,n_{\text{el}}} H_0^1(\Omega^e)$$

In our case, the estimated error may be described as

$$u'(x) = -\int_0^l g'(x,y)(\mathcal{L}\bar{u} - f)(y)\, \mathrm{d}\Omega_y \tag{27}$$

It is observed that $\mathcal{L}\bar{u} - f = -f$ since the shape functions are piecewise linear. In addition, the residual term can be decomposed in Taylor series around the center of the element, $x = c$,

$$\begin{aligned} f = \quad & f_0 \sin(2^m \pi c) + 2^m \pi f_0 \cos(2^m \pi c)(x-c) - \\ & - \frac{(2^m \pi)^2}{2} f_0 \sin(2^m \pi c)(x-c)^2 + \cdots \end{aligned} \tag{28}$$

3.1. Fine-scale Green's function. The fine-scale Green's function, $g'(x,y)$, that appears in Eq. (27), has been obtained via Eq. (8). For that purpose, it is necessary to define a fine mesh and a coarse mesh. In a (0,1) domain, we have selected a uniform coarse mesh of 10 elements and a fine mesh of 1000 elements. In Fig. 2 it is depicted the fine-scale Green's function with $EA = 1$ at the point $y = 0.48$.

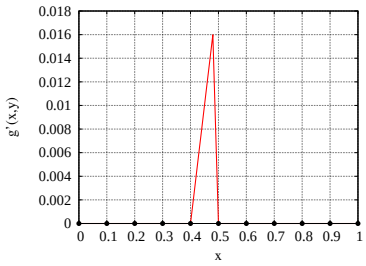

FIGURE 2. 1-D axially loaded beam. Fine-scale Green's function at $y = 0.48$ and $EA = 1$.

As Fig. 2 shows, the fine-scale Green's function is local since it is zero out of the element in which it is applied the concentrated unit-area source term, $\delta(x-y)$. In this case, the fine-scale Green's function is completely defined in the element that goes from 0.4 to 0.5.

This fine-scale Green's function can also be obtained analytically solving the differential equation below. Since this function is defined within the element, we can identify $g'(x,y) = g^e(x,y)$, where $g^e(x,y)$ is termed the *elemental Green's function* [17],

$$\begin{cases} EA\dfrac{d^2 g^e(x,y)}{dx^2} = \delta(x-y) & \text{in } \Omega^e \\ g^e(x,y) = 0 & \text{on } \Gamma_g^e \end{cases} \tag{29}$$

The result is

$$g^e(x,y) = \begin{cases} \dfrac{1}{EAh_e}(h_e - x)y & x > y \\ \dfrac{1}{EAh_e}x(h_e - y) & x < y \end{cases} \qquad x, y \in [0, h_e] \tag{30}$$

3.2. Pointwise error. As for pointwise error, the points where the error is evaluated are represented in Fig. 3. These points are used both in axially loaded beam problem and in Euler-Bernoulli examples.

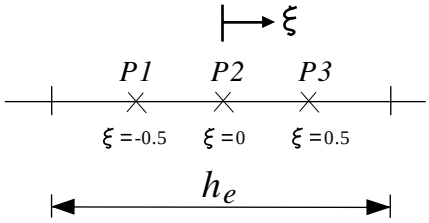

FIGURE 3. Points where the pointwise error in an element is estimated

According to Eq.(16) the pointwise error may be described by the Taylor series

$$\begin{aligned} u'(x) &= b_0^e(x) f(c) + \sum_{k=1}^{\infty} b_k^e(x) \frac{1}{k!} \frac{d^k f}{dy^k}\bigg|_{y=c} \\ &= b_0^e(x) f_0 \sin(2^m \pi c) + b_1^e(x) 2^m \pi f_0 \cos(2^m \pi c) \\ &\quad + b_2^e(x) \frac{(2^m \pi)^2}{2!} f_0 \sin(2^m \pi c) + \cdots \end{aligned} \tag{31}$$

where $b_k^e(x)$ are the residual-free bubble functions of k^{th}-moment order. They have been defined in Eq. (17) and they are depicted in Fig. 4 up to the 2^{nd}-moment order.

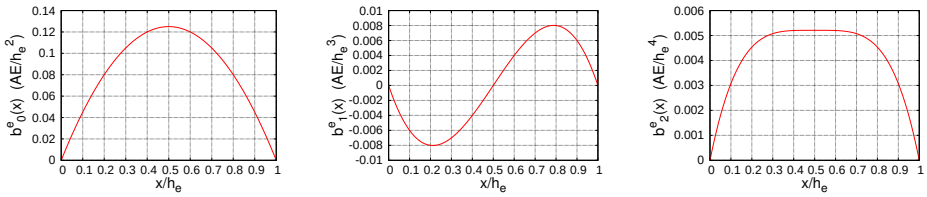

(a) $b_0^e(x)$ (b) $b_1^e(x)$ (c) $b_2^e(x)$

FIGURE 4. Graphics of the bubble functions for the axially loaded beam problem.

Finally, applying Eq. (31) we have studied the pointwise error at the three points (P1, P2, P3) of an arbitrary element (see Fig. 3). For instance, if we select a domain $\Omega = (0,1)$, $EA = 1$, $f_0 = 1$ and $m = n = 2$, we obtain a uniform mesh of 4 elements and a sinusoidal load, $f = \sin(4\pi x)$, with two cycles (see Fig. 1). Table 1 shows the pointwise error evolution and effectivity indices selecting up to

the bubble function of 9^{th} moment order. It is observed that the error estimate tends to the exact error as the number of bubble functions is increased.

TABLE 1. Pointwise error estimation for the beam loaded with an axial force.

Point	$P1$		$P2$		$P3$	
k	Error (m)	Eff.	Error (m)	Eff.	Error (m)	Eff.
0	$5.85937 \cdot 10^{-3}$	1.308536	$7.81250 \cdot 10^{-3}$	1.233701	$5.85937 \cdot 10^{-3}$	1.308536
1	$5.85937 \cdot 10^{-3}$	1.308536	$7.81250 \cdot 10^{-3}$	1.233701	$5.85937 \cdot 10^{-3}$	1.308536
2	$4.35339 \cdot 10^{-3}$	0.972215	$6.20611 \cdot 10^{-3}$	0.980030	$4.35339 \cdot 10^{-3}$	0.972215
3	$4.35339 \cdot 10^{-3}$	0.972215	$6.20611 \cdot 10^{-3}$	0.980030	$4.35339 \cdot 10^{-3}$	0.972215
4	$4.48344 \cdot 10^{-3}$	1.001258	$6.33823 \cdot 10^{-3}$	1.000893	$4.48344 \cdot 10^{-3}$	1.001258
5	$4.48344 \cdot 10^{-3}$	1.001258	$6.33823 \cdot 10^{-3}$	1.000893	$4.48344 \cdot 10^{-3}$	1.001258
6	$4.47764 \cdot 10^{-3}$	0.999963	$6.33241 \cdot 10^{-3}$	0.999974	$4.47764 \cdot 10^{-3}$	0.999963
7	$4.47764 \cdot 10^{-3}$	0.999963	$6.33241 \cdot 10^{-3}$	0.999974	$4.47764 \cdot 10^{-3}$	0.999963
8	$4.47780 \cdot 10^{-3}$	0.999999	$6.33257 \cdot 10^{-3}$	0.999999	$4.47780 \cdot 10^{-3}$	0.999999
9	$4.47780 \cdot 10^{-3}$	0.999999	$6.33257 \cdot 10^{-3}$	0.999999	$4.47780 \cdot 10^{-3}$	0.999999
E*	$4.47780 \cdot 10^{-3}$	—	$6.33257 \cdot 10^{-3}$	—	$4.47780 \cdot 10^{-3}$	—

*E stands for "Exact error".

3.3. Local error estimates. Typically, it is also practical to analyse the error in each element. Thus, recalling Eq. (19) and replacing the generic Z-norm with the L^1-norm, the L^2-norm and the H^1-seminorm,

$$
\begin{aligned}
||u'(x)||_{L^1(\Omega^e)} \leq\ & \text{meas}(\Omega^e)\tau^0_{L^1}\,|f_0 \sin(2^m \pi c)| + \\
& \sum_{k=1}^{\infty} \text{meas}(\Omega^e)\tau^k_{L^1}\frac{1}{k!}\left|\frac{d^k}{dy^k}(f_0 \sin(2^m \pi y))\right|_{y=c}\Bigg| \\
||u'(x)||_{L^2(\Omega^e)} \leq\ & \text{meas}(\Omega^e)^{1/2}\tau^0_{L^2}\,|f_0 \sin(2^m \pi c)| + \\
& \sum_{k=1}^{\infty} \text{meas}(\Omega^e)^{1/2}\tau^k_{L^2}\frac{1}{k!}\left|\frac{d^k}{dy^k}(f_0 \sin(2^m \pi y))\right|_{y=c}\Bigg| \\
||u'(x)||_{H^1(\Omega^e)} \leq\ & \text{meas}(\Omega^e)^{1/2}\tau^0_{H^1}\,|f_0 \sin(2^m \pi c)| + \\
& \sum_{k=1}^{\infty} \text{meas}(\Omega^e)^{1/2}\tau^k_{H^1}\frac{1}{k!}\left|\frac{d^k}{dy^k}(f_0 \sin(2^m \pi y))\right|_{y=c}\Bigg|
\end{aligned}
\tag{32}
$$

where c is the element centre.

We have selected the intrinsic time scales, τ^k_Z, from 0^{th}-order to 9^{th}-order (see Table 2). The higher the order of the residual, the more orders that must be taken into consideration to obtain a suitable error estimation.

The exact error in each element equals

$$
\begin{aligned}
||u'(x)_{\text{exact}}||_{L^1(\Omega^e)} &= 1.00786 \cdot 10^{-3}\ \ \text{m} \cdot \text{m} \\
||u'(x)_{\text{exact}}||_{L^2(\Omega^e)} &= 2.23890 \cdot 10^{-3}\ \ \text{m} \cdot \sqrt{\text{m}} \\
||u'(x)_{\text{exact}}||_{H^1(\Omega^e)} &= 2.81348 \cdot 10^{-02}\ \ \sqrt{\text{m}}
\end{aligned}
\tag{33}
$$

The elemental error estimate and the global effectivity are represented in Table 3. It can be seen that the error estimation is an upper bound of the error. The error has been calculated using error time-scales, τ^k_Z, up to ninth order.

TABLE 2. Error time-scales for the axially loaded beam.

τ_Z^k Order(k)	Norms L^1	L^2	H^1
0	$\frac{h^2}{12EA}$	$\frac{h^2}{\sqrt{120}EA}$	$\frac{h^1}{\sqrt{12}EA}$
1	$\frac{h^3}{192EA}$	$\frac{h^3}{\sqrt{30240}EA}$	$\frac{h^2}{\sqrt{720}EA}$
2	$\frac{h^4}{240EA}$	$\frac{h^4}{\sqrt{51840}EA}$	$\frac{h^3}{\sqrt{4032}EA}$
3	$\frac{h^5}{1920EA}$	$\frac{h^5}{\sqrt{2956800}EA}$	$\frac{h^4}{\sqrt{57600}EA}$
4	$\frac{h^6}{2240EA}$	$\frac{h^6}{\sqrt{4659200}EA}$	$\frac{h^5}{\sqrt{281600}EA}$
5	$\frac{h^7}{14336EA}$	$\frac{h^7}{\sqrt{162570240}EA}$	$\frac{h^6}{\sqrt{2609152}EA}$
6	$\frac{h^8}{16128EA}$	$\frac{h^8}{\sqrt{245661696}EA}$	$\frac{h^7}{\sqrt{12042240}EA}$
7	$\frac{h^9}{92160EA}$	$\frac{h^9}{\sqrt{6656753664}EA}$	$\frac{h^8}{\sqrt{90243072}EA}$
8	$\frac{h^{10}}{101376EA}$	$\frac{h^{10}}{\sqrt{9809952768}EA}$	$\frac{h^9}{\sqrt{403439616}EA}$
9	$\frac{h^{11}}{540672EA}$	$\frac{h^{11}}{\sqrt{227618586624}EA}$	$\frac{h^{10}}{\sqrt{2664431616}EA}$

(Note: The units for h, E and A must be expressed in SI. h is the element size)

TABLE 3. Elemental error estimation of beam loaded with an axial force.

Norm	Error units	Exact error	Estim. error	Eff.
L^1	$\mathrm{m}\cdot\mathrm{m}$	$1.00786\cdot10^{-03}$	$1.65511\cdot10^{-03}$	1.6422
L^2	$\mathrm{m}\cdot\sqrt{\mathrm{m}}$	$2.23890\cdot10^{-03}$	$3.47197\cdot10^{-03}$	1.5507
H^1	$\sqrt{\mathrm{m}}$	$2.81348\cdot10^{-02}$	$4.05022\cdot10^{-02}$	1.4396

4. Euler-Bernoulli beam problem

This section is devoted to study error estimation for the Euler-Bernoulli beam theory, which is a 4^{th}-order ordinary differential equation. The strong form, which expresses the equilibrium equation and the boundary conditions, reads:

Given the distributed transversal load $q:\Omega\to\mathbb{R}$, find $u(x):\Omega\to\mathbb{R}$ such that

$$\left\{\begin{array}{rlll} EI\dfrac{d^4u(x)}{dx^4} &= q & \text{in} & \Omega \\ u &= g & \text{on} & \Gamma_g \\ u_{,x} &= h & \text{on} & \Gamma_g \\ EIu_{,xx} &= M & \text{on} & \Gamma_h \\ EIu_{,xxx} &= Q & \text{on} & \Gamma_h \end{array}\right. \tag{34}$$

The unknown function $u(x)$ represents the deflection of the beam, E is the elastic modulus and I is the second moment of area. In the above formulation, E and I are assumed to be constants. As regards the boundary conditions, g and h are the fixed degrees of freedom for displacements and for rotation, respectively. Also, M and Q are the prescribed moment and shear force, respectively.

The weak form of the problem is obtained integrating by parts,

$$a(w,u)=(w,q) \tag{35}$$

where

$$\begin{aligned} a(w,u) &= \int_0^l w_{,xx}EIu_{,xx}\mathrm{d}x - w_{,x}M|_{\Gamma_h} - wQ|_{\Gamma_h} \\ (w,q) &= \int_0^l wq\ \ \mathrm{d}x \end{aligned} \tag{36}$$

According to the weak form, the spaces $\mathcal{S}^h \subset H^2(\Omega)$ and $\mathcal{V}^h \subset H^2(\Omega)$ must be selected. Likewise, in order to guarantee the continuity of the functions and their first derivatives in $\mathcal{S}^h$ and $\mathcal{V}^h$, C^1 functions must be employed,

$$\begin{aligned} \mathcal{S}^h &= \{u_h \in (H^2(\Omega)) \mid u_{h|\Omega^e} \in \mathbb{P}_k, u_{h|\Gamma_g} = g, u_{h,x|\Gamma_g} = h, \forall \Omega^e \in \widetilde{\Omega}\} \\ \mathcal{V}^h &= \{w_h \in (H^2(\Omega)) \mid w_{h|\Omega^e} \in \mathbb{P}_k, w_{h|\Gamma_g} = 0, w_{h,x|\Gamma_g} = 0, \forall \Omega^e \in \widetilde{\Omega}\} \end{aligned} \tag{37}$$

where $\mathbb{P}_k$ are the polynomial of degree at most k. Therefore, using the standard Galerkin method, the FEM problem reads:

Find $u_h \in \mathcal{S}^h$ such that

$$a(v_h, u_h) = (v_h, f) + (v_h, h)_{\Gamma_h} \qquad \forall v_h \in \mathcal{V}^h \tag{38}$$

Remark 1. The same theory can also be applied to similar problems such as rectangular plates with infinite length, $\frac{d^4 w(x)}{dx^4} = \frac{q}{D}$ where $w(x)$ is the vertical displacement, q the distributed load and D the plate rigidity.

4.1. Elements considered in the analysis. In order to approximate the solution, two elements (Element 1 and Element 2) are employed with C^1-continuity, i.e., with continuously differentiable displacements.

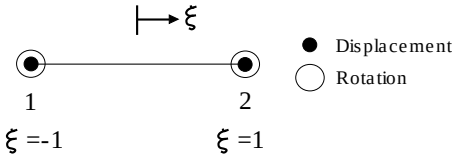

FIGURE 5. Element 1: Element with two nodes.

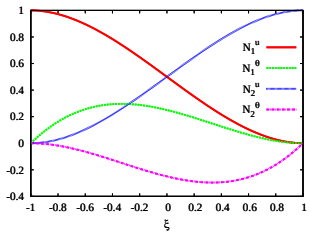

FIGURE 6. Element 1: Shape functions associated with the nodal variables.

4.1.1. Element 1. The first element contains the piecewise cubic Hermite shape functions with two nodes in each element (see Fig. 5). In each node both the displacement, N_i^u, and the rotation, N_i^θ are defined. The numerical solution in a reference element, $u_{h_{E1}}(x)$, is expressed by the formula:

$$u_{h_{E1}} = N_1^u u_1 + N_1^\theta \theta_1 + N_2^u u_2 + N_2^\theta \theta_2 \tag{39}$$

where

$$\begin{aligned} N_1^u(\xi) &= \frac{1}{4}(2 - 3\xi + \xi^3) \qquad & N_1^\theta(\xi) &= \frac{1}{4}(1 - \xi - \xi^2 + \xi^3) \\ N_2^u(\xi) &= \frac{1}{4}(2 + 3\xi - \xi^3) \qquad & N_2^\theta(\xi) &= \frac{1}{4}(-1 - \xi + \xi^2 + \xi^3) \end{aligned} \tag{40}$$

with ξ being the reference coordinate.

The shape functions, N_1^u, N_2^u, N_1^θ and N_2^θ, are represented in Fig. 6 in the reference element.

4.1.2. Element 2. In the second element, we add a central node associated with a displacement function, N_i^u (see Fig. 7). The shape functions are represented in Fig. 8. The central node has associated a bubble function as shape function and it will be shown that it has a relevant importance in the error.

Remark 2. If we add to the central node the rotation degree of freedom, we recover Element 1.

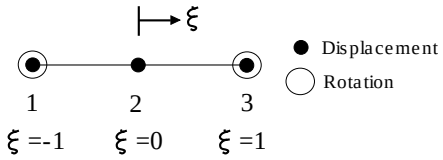

FIGURE 7. Element 2: Element with three nodes.

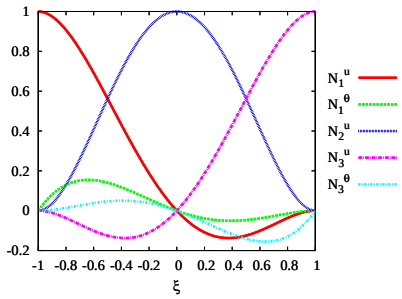

FIGURE 8. Element 2: Shape functions associated with the nodal variables.

The numerical solution, $u_{h_{E2}}(x)$ in an element, is expressed by the formula:

$$u_{h_{E2}} = N_1^u u_1 + N_1^\theta \theta_1 + N_2^u u_2 + N_3^u u_3 + N_3^\theta \theta_3 \tag{41}$$

Using the reference element, the shape functions are

$$\begin{aligned} N_1^u(\xi) &= -\frac{\xi^4}{2} + \frac{\xi^3}{4} + \xi^2 - \frac{3\xi}{4} \\ N_1^\theta(\xi) &= -\frac{\xi^4}{4} + \frac{\xi^3}{4} + \frac{\xi^2}{4} - \frac{\xi}{4} \\ N_2^u(\xi) &= \xi^4 - 2\xi^2 + 1 \\ N_3^u(\xi) &= -\frac{\xi^4}{2} - \frac{\xi^3}{4} + \xi^2 + \frac{3\xi}{4} \\ N_3^\theta(\xi) &= \frac{\xi^4}{4} + \frac{\xi^3}{4} - \frac{\xi^2}{4} - \frac{\xi}{4} \end{aligned} \tag{42}$$

4.2. Example problems. The proposed problems consist of a beam with various loads, q, and boundary conditions. The first problem, which is termed Problem 1, is a beam with a uniform load and fixed displacements at both ends (see Fig. 9a). The second one, Problem 2, is a cantilever beam with a triangular load distribution (Fig. 9b).

For the numerical analysis, it has been chosen $L = 10$ m and $EI = 40000$ N/m for both problems. The load for Problem 1 is $q = 100$ N/m and for Problem 2

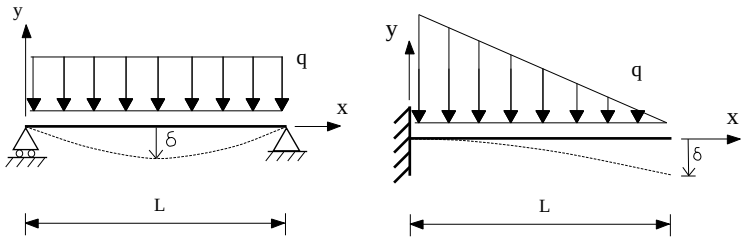

(a) Prob. 1: Supported beam at both ends with a uniform load

(b) Prob. 2: Cantilever beam with a triangular load

FIGURE 9. Benchmarks for Euler-Bernoulli problems.

is $q = 1000\frac{1-x}{L}$ N/m. The simulations are carried out on uniform meshes. These problems have the following analytical solutions, which can be taken advantage of to calculate the exact error of the FEM,

$$\begin{aligned} &\text{Prob. 1:} \quad u(x)_{\text{Prob1}} = \frac{qx}{24EI}(x^3 - 2Lx^2 + L^3) \\ &\text{Prob. 2:} \quad u(x)_{\text{Prob2}} = \frac{(L-x)^2}{24EI}q(0)\left(\frac{-(L-x)^3}{5L} - 2L(L-x) + 4L^2\right) \end{aligned} \tag{43}$$

4.3. Error expressions for the Euler-Bernoulli beam. The *pointwise error* can be determined by means of bubble functions. Applying Eq. (16) to the Euler-Bernoulli problem results in

$$\begin{aligned} u'(x) = \; & b_0^e(x)(EI\frac{d^4\bar{u}(y)}{dy^4} - q)(c) + \\ & \sum_{k=1}^{\infty} b_k^e(y)\frac{1}{k!}\frac{d^k}{dy^k}(EI\frac{d^4\bar{u}(x)}{dy^4} - q)\Big|_{y=c} \end{aligned} \tag{44}$$

Also, for these problems, we can measure the error in the whole domain and in the elements making use of the L^1-norm, L^2-norm and H^1-seminorm. For the Euler-Bernoulli beam problem, the elemental error estimate (19) may be rewritten as

$$\begin{aligned} ||u'(x)||_{L^1(\Omega^e)} \leq \; & \text{meas}(\Omega^e)\tau_{L^1}^0 \left|(EI\frac{d^4\bar{u}(y)}{dy^4} - q)(c)\right| + \\ & \sum_{k=1}^{\infty} \text{meas}(\Omega^e)\tau_{L^1}^k \frac{1}{k!}\left|\frac{d^k}{dy^k}(EI\frac{d^4\bar{u}(y)}{dy^4} - q)\Big|_{y=c}\right| \\ ||u'(x)||_{L^2(\Omega^e)} \leq \; & \text{meas}(\Omega^e)^{1/2}\tau_{L^2}^0 \left|(EI\frac{d^4\bar{u}(y)}{dy^4} - q)(c)\right| + \\ & \sum_{k=1}^{\infty} \text{meas}(\Omega^e)^{1/2}\tau_{L^2}^k \frac{1}{k!}\left|\frac{d^k}{dy^k}(EI\frac{d^4\bar{u}(y)}{dy^4} - q)\Big|_{y=c}\right| \\ ||u'(x)||_{H^1(\Omega^e)} \leq \; & \text{meas}(\Omega^e)^{1/2}\tau_{H^1}^0 \left|(EI\frac{d^4\bar{u}(y)}{dy^4} - q)(c)\right| + \\ & \sum_{k=1}^{\infty} \text{meas}(\Omega^e)^{1/2}\tau_{H^1}^k \frac{1}{k!}\left|\frac{d^k}{dy^k}(EI\frac{d^4\bar{u}(y)}{dy^4} - q)\Big|_{y=c}\right| \end{aligned} \tag{45}$$

where c is the centre of the element. Normally, the residual is not a polynomial of high degree. A typical case is when the residual is piecewise constant. In this case the above equations can be reduced to the simpler expressions,

$$
\begin{aligned}
||u'(x)||_{L^1(\Omega^e)} &= \text{meas}(\Omega^e)\ \tau^0_{L^1} \left|(EI\frac{d^4\bar{u}(y)}{dy^4} - q)(c)\right| \\
||u'(x)||_{L^2(\Omega^e)} &= \text{meas}(\Omega^e)^{1/2}\ \tau^0_{L^2} \left|(EI\frac{d^4\bar{u}(y)}{dy^4} - q)(c)\right| \\
||u'(x)||_{H^1(\Omega^e)} &= \text{meas}(\Omega^e)^{1/2}\ \tau^0_{H^1} \left|(EI\frac{d^4\bar{u}(y)}{dy^4} - q)(c)\right|
\end{aligned}
\tag{46}
$$

In the next sections, the intrinsic error scales τ which appear in Eqs. (45) and (46) are defined.

It is important to take into consideration that the error scales depend strongly on the element type. It can be proved that the numerical solution and its first derivative is nodally exact [25]. Therefore, the fine-scale Green's function $g'(x,y)$ is zero at the nodes and the error is confined within each element. This property can be confirmed computing the fine-scales as proposed Hughes and Sangalli [27].

4.4. Analysis for Element 1. The fine-scale Green's function for Element 1 is shown in Fig. 10. It can be appreciated the local character of $g'(x,y)$. To obtain the fine-scale Green's function, the (0,1)-domain is associated with a uniform coarse mesh of 10 elements and a uniform fine mesh of 1000 elements. The fine-scale Green's function is represented in Fig. 10 at $y = 0.48$ for $EI = 1$. It can be seen that $g'(x,y)$ is confined within the element.

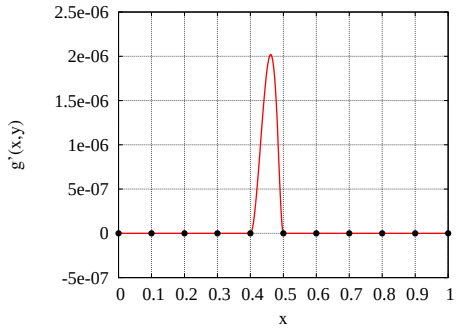

FIGURE 10. Euler-Bernoulli problem. Fine-scale Green's function for Element 1 and $EI = 1$.

Therefore, we can establish that $g'(x,y) = g^e(x,y)$, where $g^e(x,y)$ is the *element Green's function*. The value of $g^e(x,y)$ is only different from zero when x and y belong to the same element. Therefore, the error can be calculated in each element without taking into account the error source of other elements.

Another way of obtaining $g^e(x,y)$ for Element 1 is solving within each element the corresponding element Green's function problem, in which there are only homogeneous Dirichlet boundary conditions,

$$
\begin{cases}
EI\dfrac{d^4 g^e(x,y)}{dx^4} = \delta(x-y) & \text{in} \quad \Omega^e \\
g^e(x,y) = 0 & \text{on} \quad \Gamma^e \\
g^e_{,x}(x,y) = 0 & \text{on} \quad \Gamma^e
\end{cases}
\tag{47}
$$

In Eq. (47), Ω^e is the element domain, Γ^e the element boundary and $\delta(x,y)$ the Dirac delta distribution. Fig. 11 depicts $g^e(x,y)$ for several values of the coordinate y. Note that the fine-scale Green's functions are the same for both methods.

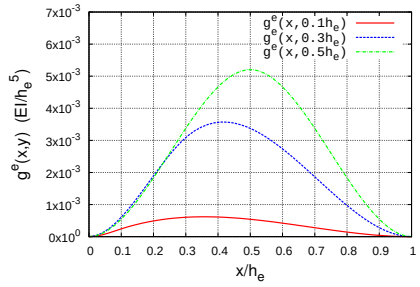

FIGURE 11. Euler-Bernoulli problem. Green's functions for several coordinates.

The solution of (47) is given by the following Green's function, $x, y \in [0, h_e]$

$$g^e(x,y) = \begin{cases} \dfrac{y^2}{6EI}\dfrac{(h_e-x)^2}{h_e^2}\left(2h_e - y + x - 2(h_e-y)\dfrac{h_e-x}{h_e}\right) & x > y \\ \dfrac{(h_e-y)^2}{6EI}\dfrac{x^2}{h_e^2}(3y - x - \dfrac{2yx}{h_e}) & x < y \end{cases} \tag{48}$$

In this case, the fine-scale space $\mathcal{S}'$ is the space of bubbles functions belonging to $H_0^2(\Omega)$

$$\mathcal{S}' = \bigoplus_{e=1,\ldots,n_{\text{el}}} H_0^2(\Omega^e)$$

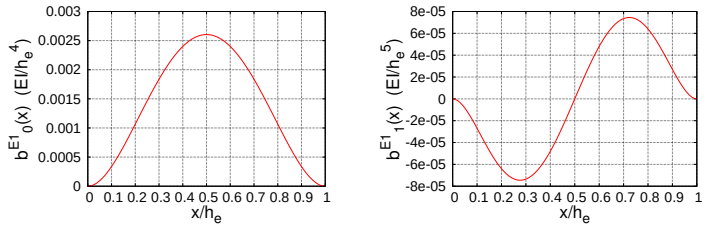

(a) $b_0^{E1}(x)$ (b) $b_1^{E1}(x)$

FIGURE 12. Euler-Bernoulli problem. Graphics of the bubble functions for Element 1.

The bubble functions for the Euler-Bernoulli beam problem are represented in Fig. 12. In order to quantify the bubble function value for error estimation, we

employ the L^1-norm, L^2-norm and the H^1-seminorm in each element,

$$\begin{aligned} \left|\left|b_0^{E1}(x)\right|\right|_{L^1(\Omega^e)} &= \frac{h_e^5}{720EI} \\ \left|\left|b_0^{E1}(x)\right|\right|_{L^2(\Omega^e)} &= \frac{h_e^{9/2}}{72\sqrt{70}EI} \\ \left|\left|b_0^{E1}(x)\right|\right|_{H^1(\Omega^e)} &= \frac{h_e^{7/2}}{12\sqrt{210}EI} \end{aligned} \tag{49}$$

The superscript $E1$ refers to Element 1. Finally, the intrinsic scales $\tau^0_{L^1}$, $\tau^0_{L^2}$ and $\tau^0_{H^1}$ in Eq. (46) take the form

$$\begin{aligned} \tau_{L^1}^{E1,0} &= \frac{||b_0^e(x)||_{L^1(\Omega^e)}}{\text{meas}(\Omega^e)} = \frac{h_e^4}{720EI} \\ \tau_{L^2}^{E1,0} &= \frac{||b_0^e(x)||_{L^2(\Omega^e)}}{\text{meas}(\Omega^e)^{1/2}} = \frac{h_e^4}{72\sqrt{70}EI} \\ \tau_{H^1}^{E1,0} &= \frac{||b_0^e(x)||_{H^1(\Omega^e)}}{\text{meas}(\Omega^e)^{1/2}} = \frac{h_e^3}{12\sqrt{210}EI} \end{aligned} \tag{50}$$

In case that the residual is not piecewise constant, we can approximate it by Taylor series as above, leading to bubble functions and time scales of higher order.

In Prob. 2, the residual is piecewise linear, so it is enough to define the bubble functions and the time scales of first order,

$$\begin{aligned} \left|\left|b_1^{E1}(x)\right|\right|_{L^1(\Omega^e)} &= \frac{h_e^6}{23040EI} \\ \left|\left|b_1^{E1}(x)\right|\right|_{L^2(\Omega^e)} &= \frac{h_e^{11/2}}{720\sqrt{770}EI} \\ \left|\left|b_1^{E1}(x)\right|\right|_{H^1(\Omega^e)} &= \frac{h_e^{9/2}}{360\sqrt{70}EI} \end{aligned} \tag{51}$$

$$\begin{aligned} \tau_{L^1}^{E1,1} &= \frac{\left|\left|b_1^{E1}(x)\right|\right|_{L^1(\Omega^e)}}{\text{meas}(\Omega^e)} = \frac{h_e^5}{23040EI} \\ \tau_{L^2}^{E1,1} &= \frac{\left|\left|b_1^{E1}(x)\right|\right|_{L^2(\Omega^e)}}{\text{meas}(\Omega^e)^{1/2}} = \frac{h_e^5}{720\sqrt{770}EI} \\ \tau_{H^1}^{E1,1} &= \frac{\left|\left|b_1^{E1}(x)\right|\right|_{H^1(\Omega^e)}}{\text{meas}(\Omega^e)^{1/2}} = \frac{h_e^4}{360\sqrt{70}EI} \end{aligned} \tag{52}$$

4.4.1. Results for Problem 1. In this problem the residual is piecewise constant, $\frac{d^4\bar{u}(x)}{dx^4} - q \in \mathbb{P}_0$. Furthermore, $\frac{d^4\bar{u}(x)}{dx^4} = 0$. Therefore, the elemental error can be determined by Eq. (46).

Fig. 13 shows the efficiency of the estimator for different number of elements. In this case both the local and global effectivities are one, i.e., the estimated error is the same as the exact error.

The error convergence rates which are achieved with Element 1 are studied in Fig. 14, where the error in the central element is represented. The convergence rates of the elemental error in each norm are steered by the norms of the bubble functions, see Eq. (49). Furthermore, these convergence rates are in concordance

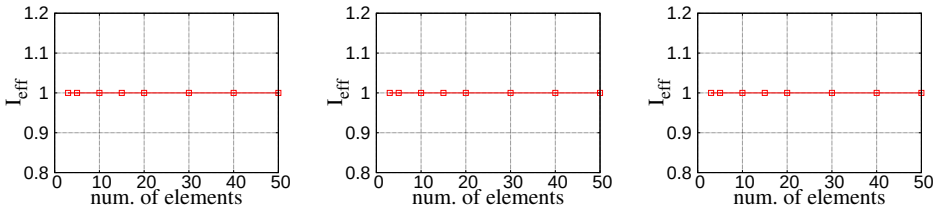

(a) L^1-norm (b) L^2-norm (c) H^1-seminorm

FIGURE 13. Global effectivity for Problem 1 and Element 1.

with the theory, which must be adapted to the elemental error (see, for instance, Chapter 4 of [25]).

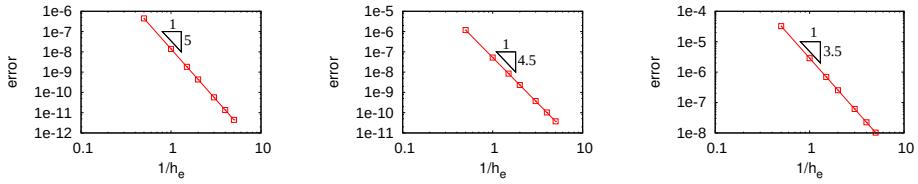

(a) L^1-norm (b) L^2-norm (c) H^1-seminorm

FIGURE 14. Elemental error for Problem 1 and Element 1.

Eventually, the pointwise error is studied in Table 4. The error is evaluated at points P1, P2 and P3 (see Fig. 3). It can be seen that the error estimate is exact.

TABLE 4. Pointwise error estimation of Euler-Bernoulli problem. Element 1 and Problem 1.

Point	Exact error (m)	Estimated error (m)
P1	$5.859375 \cdot 10^{-5}$	$5.859375 \cdot 10^{-5}$
P2	$1.041667 \cdot 10^{-4}$	$1.041667 \cdot 10^{-4}$
P3	$5.859375 \cdot 10^{-5}$	$5.859375 \cdot 10^{-5}$

4.4.2. Results for Problem 2. In Problem 2 the residual is piecewise linear. Therefore, we may approximate the residual by Taylor series and make use of Eq. (45) where only the first two contributions are non zero. The global effectivities are shown in Fig. 15. It can be seen that the effectivities tend to the desired unit value as the number of element is increased.

In this case, although the effectivities are close to one, they are not exact due to the Taylor series approximation. The elemental error convergence measured in different norms is shown in Fig. 16.

Finally, Table 5 shows the pointwise error. Again, the error estimate is exact.

4.5. Analysis for Element 2. Owing to its central node, Element 2 is more precise than Element 1. This aspect makes the fine-scale Green's function associated with Element 2 significantly different from that of Element 1. In this case, the fine-scale Green's function of Fig. 17 has been calculated in a uniform coarse mesh of

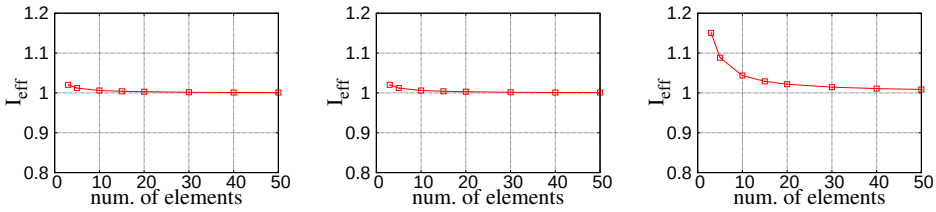

(a) L^1-norm (b) L^2-norm (c) H^1-seminorm

FIGURE 15. Global effectivity for Problem 2 and Element 1.

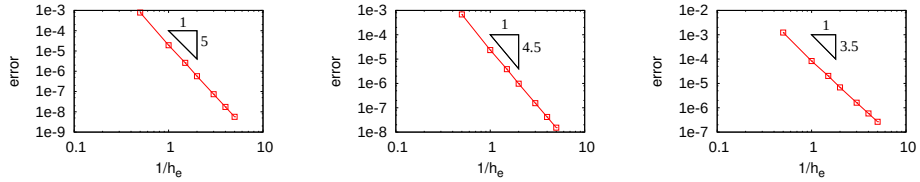

(a) L^1-norm (b) L^2-norm (c) H^1-seminorm

FIGURE 16. Elemental error for Problem 2 and Element 1.

TABLE 5. Pointwise error estimation of Euler-Bernoulli problem. Element 1 and Problem 2.

Point	Exact error (m)	Estimated error (m)
P1	$2.988281 \cdot 10^{-4}$	$2.988281 \cdot 10^{-4}$
P2	$5.208333 \cdot 10^{-4}$	$5.208333 \cdot 10^{-4}$
P3	$2.871094 \cdot 10^{-4}$	$2.871094 \cdot 10^{-4}$

5 elements and a uniform fine mesh of 1000 elements. Fig. 17 depicts $g'(x, y)$ for $EI = 1$ at different points of the central element. It is evaluated in the central element which is defined in the interval (0.4,0.6). It is appreciated that $g'(x, y)$ is completely local in the element. Fig. 17 shows that the fine-scale Green's function is different from zero at the central node. This means that the error can be different from zero at the central node, in spite of being zero at the inter-element nodes.

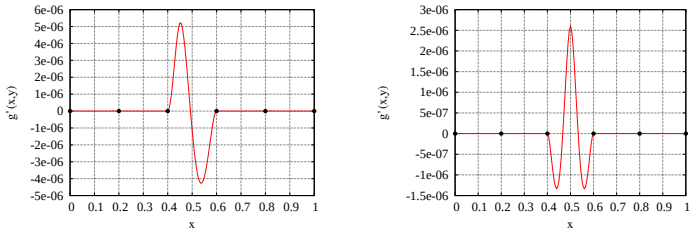

(a) y=0.45 (b) y=0.50

FIGURE 17. Euler-Bernoulli problem. Fine-scale Green's functions for Element 2 and $EI = 1$.

In this element, the fine-scale space is a subset of bubble functions belonging to $H_0^2(\Omega)$, due to the central node introducing a bubble function,

$$\mathcal{S}' \subset \bigoplus_{e=1,\ldots,n_{\text{el}}} H_0^2(\Omega^e)$$

Whereas for Element 1 we are able to obtain the fine-scale Green's functions via two different methods, for Element 2 we can only obtain $g'(x,y)$ by means of the Hughes-Sangalli formulae. Again, as explained for Element 1, we can define the bubble functions and the intrinsic scales associated with the fine-scale Green's function of Fig. 17. The bubble functions are necessarily obtained by numerical integration.

A relevant aspect in this element is that the bubble function of 0^{th}-moment order, $b_0^{E2}(x)$, is zero. Therefore, the intrinsic error scales of 0^{th}-moment order are also zero. The following expressions show the bubble functions of higher order measured in different norms,

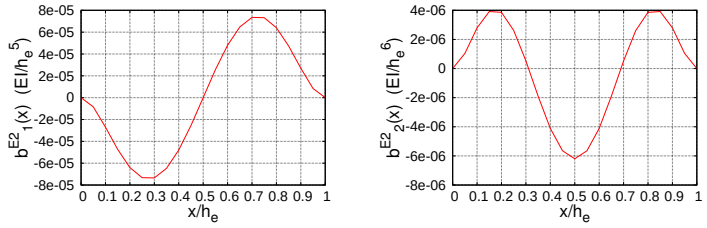

(a) $b_1^{E2}(x)$ (b) $b_2^{E2}(x)$

FIGURE 18. Graphics of the bubble functions for Euler-Bernoulli beam and Element 2.

$$\begin{aligned}
\left|\left|b_1^{E2}(x)\right|\right|_{L^1(\Omega^e)} &= 4.339475 \cdot 10^{-5} \frac{h_e^6}{EI} \\
\left|\left|b_1^{E2}(x)\right|\right|_{L^2(\Omega^e)} &= 5.010625 \cdot 10^{-5} \frac{h_e^{5.5}}{EI} \\
\left|\left|b_1^{E2}(x)\right|\right|_{H^1(\Omega^e)} &= 3.327346 \cdot 10^{-4} \frac{h_e^{4.5}}{EI}
\end{aligned} \tag{53}$$

$$\begin{aligned}
\left|\left|b_2^{E2}(x)\right|\right|_{L^1(\Omega^e)} &= 2.951922 \cdot 10^{-6} \frac{h_e^7}{EI} \\
\left|\left|b_2^{E2}(x)\right|\right|_{L^2(\Omega^e)} &= 3.449933 \cdot 10^{-6} \frac{h_e^{6.5}}{EI} \\
\left|\left|b_2^{E2}(x)\right|\right|_{H^1(\Omega^e)} &= 3.222477 \cdot 10^{-5} \frac{h_e^{5.5}}{EI}
\end{aligned} \tag{54}$$

The superscript $E2$ refers to Element 2. The intrinsic error scales can be written as

$$
\begin{aligned}
\tau_{L^1}^{E2,1} &= \frac{||b_1^e(x)||_{L^1(\Omega^e)}}{\text{meas}(\Omega^e)} = 4.339475 \cdot 10^{-5} \frac{h_e^5}{EI} \\
\tau_{L^2}^{E2,1} &= \frac{||b_1^e(x)||_{L^2(\Omega^e)}}{\text{meas}(\Omega^e)^{1/2}} = 5.010625 \cdot 10^{-5} \frac{h_e^5}{EI} \\
\tau_{H^1}^{E2,1} &= \frac{||b_1^e(x)||_{H^1(\Omega^e)}}{\text{meas}(\Omega^e)^{1/2}} = 3.327346 \cdot 10^{-4} \frac{h_e^4}{EI} \\
\tau_{L^1}^{E2,2} &= \frac{||b_2^e(x)||_{L^1(\Omega^e)}}{\text{meas}(\Omega^e)} = 2.951922 \cdot 10^{-6} \frac{h_e^6}{EI} \\
\tau_{L^2}^{E2,2} &= \frac{||b_2^e(x)||_{L^2(\Omega^e)}}{\text{meas}(\Omega^e)^{1/2}} = 3.449933 \cdot 10^{-6} \frac{h_e^6}{EI} \\
\tau_{H^1}^{E2,2} &= \frac{||b_2^e(x)||_{H^1(\Omega^e)}}{\text{meas}(\Omega^e)^{1/2}} = 3.222477 \cdot 10^{-5} \frac{h_e^5}{EI}
\end{aligned}
\tag{55}
$$

These bubble functions are depicted in Fig. 18. In this case, we represent the 1st- and 2nd-order moment, although in the proposed examples, the first-order moment is enough for the calculations.

Remark 3. Since for Element 2 the 0th-order bubble function is zero, the error source due to the constant part of the residual, $b_0^e(x)(EI\frac{d^4\bar{u}(x)}{dx^4} - q)(c)$ vanishes (see Eq. (44) or (45)). It can be proved that $g'(x,y)$ is L^2-orthogonal to residuals belonging to $\mathbb{P}_{k-4}$. This idea was proved by Hughes and Sangalli in [27] for the transport equation (2nd-order ODE) where $g'(x,y)$ is orthogonal to residuals belonging to $\mathbb{P}_{k-2}$

Remark 4. Observe that the first order bubble functions for Element 1, $b_1^{E1}(x)$, and Element 2, $b_1^{E2}(x)$, are the same (see Figs. 12 and 18). Therefore, the advantage of Element 2 over Element 1 is that it gets rid of the 0th-order source error component.

4.5.1. Results for Problem 1. As mentioned in Remark 3, the intrinsic error scales of 0th-order moment are zero. Therefore, there is not error for constant loads, that is to say, the FEM solution equals the analytical solution.

4.5.2. Results for Problem 2. In this problem, the residual is piecewise linear. In order to estimate the error is enough to handle the 1st-order moment of the intrinsic error scales. In Fig. 19, the efficiency index is depicted in the three analysed norms. It is observed that it is one irrespective of the number of the elements. Thus, the predicted error is the same as the exact one.

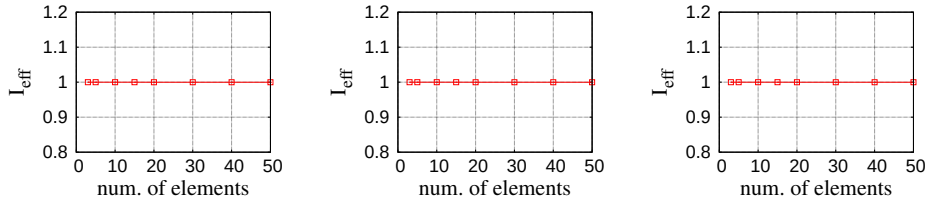

(a) L^1-norm (b) L^2-norm (c) H^1-seminorm

FIGURE 19. Global effectivity for Problem 2 and Element 2.

Fig. 20 expresses the evolution of the elemental error with the number of elements in the central element of the beam. It can be seen that the convergence rate is greater with Element 2 than with Element 1. As for Element 1, the convergence rates of Fig. 20 are governed by the norms of the bubble functions, see Eq. (53).

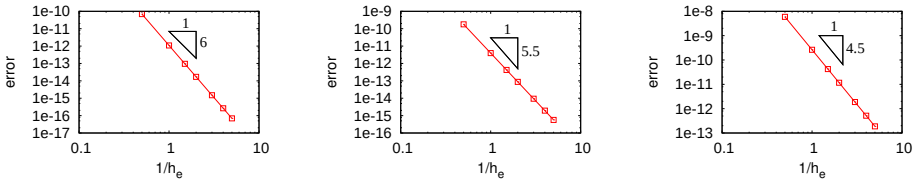

(a) L^1-norm (b) L^2-norm (c) H^1-seminorm

FIGURE 20. Elemental error for Problem 2 and Element 2.

The pointwise error is represented in Table 6. It can be observed that the error at point 2 is zero as expected and that the predicted error is once again exact.

TABLE 6. Pointwise error estimation of Euler-Bernoulli problem. Element 2 and Problem 2.

Point	Exact error (m)	Estimated error (m)
P1	$5.859376 \cdot 10^{-6}$	$5.859376 \cdot 10^{-6}$
P2	0	0
P3	$5.859376 \cdot 10^{-6}$	$5.859376 \cdot 10^{-6}$

5. Extension to multi-dimensional problems

Taking advantage of the theoretical formulation of this error estimator, the present methodology can be extended to multi-dimensional problems. In the case of pointwise error estimates, this extension would involve multi-dimensional Taylor series expansions, what gives rise to an increased number of bubble functions and more elaborate calculations. In the case of global and local (element) error estimates, the extension is straightforward [23].

One main difference between one-dimensional and multi-dimensional problems is that, in the former case, the error is usually nodally exact, whereas in the latter case, the error is not exact along element edges. Therefore, the challenge to estimate the error in multi-dimensional cases is that, beyond the local error, which has been explained in this paper, we might need to take into account the global (or pollution) error. This global error can be characterized by means of the jump operator which collects the inter-element residuals, as carried out in other manuscripts by Hauke et al. [16, 18]. Currently, we are working on this field.

6. Conclusions

This work extends previous results on a posteriori error estimation based on the variational multiscale theory to second and fourth order differential equations that can be solved using the Galerkin method. Two examples are considered, namely, the axially loaded beam and the Euler-Bernoulli beam, respectively. The theory yields exact error estimates for the pointwise error, and for local and global error

norms. For high-order residuals, upper bounds for the local and global error norms have been derived.

The paper describes in detail how to compute numerically the corresponding fine-scale and element Green's functions for any element in 2^{nd} and 4^{th}-order ODE's irrespective of the element order. From them, residual-free bubbles, intrinsic error time-scales and their moments have been calculated for various element types. The procedure can be easily extended to other elements.

The numerical examples confirm the theoretical properties of the method, which under certain conditions provides exact pointwise, local and global error estimates. Furthermore, it has been shown that the present technology succeeds when other residual-based methods fail. Therefore, the proposed a posteriori error estimator is a feasible tool for error estimation. The fact that the error estimation is explicit implies very little computational cost. That is to say, the error estimation is carried out by post-processing the FEM solution without solving other differential equations as it happens with implicit error estimators.

Acknowledgements

The authors thank G. Sangalli and F. Lizarraga for helpful conversations.

References

[1] M. Ainsworth and A. Craig, A posteriori error in the finite element method, Numer. Math., 60 (1991) 429-463.
[2] M. Ainsworth and J.T. Oden, A Posterior Error Estimation in Finite Element Analysis, John Wiley & Sons, 2000.
[3] I. Babuška and W. Rheinboldt, Adaptive approaches and reliability estimations in finite element analysis, Comput. Meth. Appl. Mech. Engrg., 17 (1979) 519-540.
[4] I. Babuska and W. Rheinboldt, Analysis of optimal finite element meshes in r^1, Math. Comp., 33 (1979) 435-463.
[5] I. Babuška and A. Miller, A feedback finite element method with a posteriori error estimation part 1, Comput. Meth. Appl. Mech. Engrg., 61 (1987) 1-40.
[6] I. M. Babuška and W. C. Rheinboldt, A posteriori error estimates for the finite element, Int. J. Numer. Methods Engrg., 12 (1978) 1597-1615.
[7] F. Brezzi, L. Franca, T. Hughes and A. Russo, $b = \int g$, Comput. Meth. Appl. Mech. Engrg., 145 (1997) 329-339.
[8] C. Carstensen and J. Thiele, Partition of unity for localization in implicit a posteriori finite element error control for elasticity, Int. J. Numer. Meth. Engng., 73 (2008) 71-95.
[9] P. Díez and A. Huerta, A posteriori error estimation for standard finite element analysis, Comput. Methods Appl. Mech. Engrg., 163 (1998) 141-157.
[10] A. ElSheik, S. Chidiac and W. Smith, A posteriori error estimation based on numerical realization of the variational multiscale method, Comput. Meth. Appl. Mech. Engrg., 197 (2008) 3637-3656.
[11] D. Estep, M. Holst and M. Larson, Generalized Green's functions and the effective domain of influence, SIAM J. Sci. comput., in press 26 (2005) 1314-1339.
[12] L. P. Franca and A. Russo, Deriving upwinding, mass lumping and selective reduced integration by residual-free bubbles, Appl. Math. Letters, 9 (1996) 83-88.
[13] L. P. Franca and A. Russo, Recovering SUPG using Petrov-Galerkin formulations enriched with adjoint residual-free bubbles, Comput. Meth. Appl. Mech. Engrg., 182 (2000) 333-339.
[14] G. Hauke and M. H. Doweidar, Intrinsic scales and a posteriori multiscale error estimation for piecewise-linear functions and residuals, Int. J. Comput. Fluid Dyn., 20 (2006) 211-222.
[15] G. Hauke, M. H. Doweidar and S. Fuentes, Mesh adaptivity for the transport equation led by variational multiscale error estimators, Int. J. Numer. Meth. Fluids, 69 (2011) 1835-1850.
[16] G. Hauke, M. H. Doweidar and D. Fuster, Multiscale multi-dimensional explicit a-posteriori error estimation for fluid dynamics. In: P. Wesseling, E. Oñate, J. Périaux (eds.) European Conference on Computational Fluid Dynamics, pp. 1–13, 2006.

[17] G. Hauke and M. H. Doweidar, D. Fuster, A. Gomez, and J. Sayas, Application of variational a-posteriori multiscale error estimation to higher-order elements, Comput. Mech., 38 (2006) 382-389.
[18] G. Hauke, M. H. Doweidar and M. Miana, The multiscale approach to error estimation and adaptivity, Comput. Meth. Appl. Mech. Engrg., 195 (2006) 1573-1593.
[19] G. Hauke, M. H. Doweidar and M. Miana, Proper intrinsic scales for a-posteriori multiscale error estimation, Comput. Meth. Appl. Mech. Engrg., 195 (2006) 3983-4001.
[20] G. Hauke and D. Fuster, Variational multiscale a-posteriori error estimation for quantities of interest, J. Appl. Mech., 76 (2009) 1-6.
[21] G. Hauke, D. Fuster and M. H. Doweidar, Variational multiscale a-posteriori error estimation for the multi-dimensional transport equation, Comput. Meth. Appl. Mech. Engrg., 197 (2008) 2701-2718.
[22] G. Hauke, D. Fuster and F. Lizarraga, Variational multiscale a-posteriori error estimation for systems: the Euler and Navier-Stokes equations, Comput. Mech., submitted.
[23] G. Hauk and D. Irisarri, Variational mutiscale a posteriori error estimation for systems. Application to linear elasticity, Comput. Meth. Appl. Mech. Engrg., submitted.
[24] T. Hughes, Multiscale phenomena: Green's functions, the Dirichlet-to-Neumann formulation, subgrid scale models, bubbles and the origins of stabilized methods, Comput. Meth. Appl. Mech. Engrg., 127 (1995) 387-401.
[25] T. Hughes, The Finite Element Method: Linear Static and Dynamic Finite Element Analysis, Dover Publications, 2000.
[26] T. Hughes, G. Feijoo, L. Mazzei and J. Quincy, The variational multiscale method: A paradigm for computational mechanics, Comput. Meth. Appl. Mech. Engrg., 166 (1998) 3-24.
[27] T. Hughes and G. Sangalli, Variational multiscale analysis: the fine-scale green's function, projection, optimization, localization and stabilized methods, SIAM J. Numer. Anal., 45 (2007) 539-557.
[28] P. Ladevèze and D. Leguillon, Error estimate procedure in the finite element method and applications, SIAM J. Numer. Anal., 20 (1983) 485-509.
[29] P. Ladevèze, P. Rougeot, P. Blanchard and J. Moreau, Local error estimator for finite element linear analysis, Comput. Methods Appl. Mech. Engrg., 176 (1999) 231-246.
[30] M. G. Larson, A. Målqvist, Adaptive variational multiscale methods based on a posteriori error estimation: Duality techniques for elliptic problems, Comput. Sci. Engrg., 44 (2005) 181-193.
[31] M. Lonsing and R. Verfürth, A posteriori error estimators for mixed finite element methods in linear elasticity, Numer. Math., 97 (2004) 757-778.
[32] A. Masud, T. Truster and L. A. Bergman, A variational multiscalei a posteriori error estimation method for mixed form of nearly incompressible elasticity, Comput. Methods Appl. Mech. Engrg., 200 (2011) 3453-3481.
[33] R. H. Nochetto, Pointwise a posteriori error estimates for elliptic problems on highly graded meshes, Math. Comp., 64 (1995) 1-22.
[34] J. T. Oden and S. Prudhomme, Goal-oriented error estimation and adaptivity for the Finite Element Methods. Comput. Methods Appl. Mech. Engrg., 111 (1994) 185-202.
[35] N. Parés, P. Díez, and A. Huerta, Subdomain-based flux-free a posteriori error estimators, Comput. Methods Appl. Mech. Engrg., 195 (2006) 297-323.
[36] S. Prudhomme and J. T. Oden, On goal-oriented error estimation for elliptic problems: application to the control of pointwise errors, Comput. Methods Appl. Mech. Engrg., 176 (1999) 313-331.
[37] S. Prudhomme, J. T. Oden, T. W. J. Bas and M. Botkin, Practical methods for a posteriori error estimation in engineering applications, Int. J. Numer. Meth. Engng., 56 (2003) 1193-1224.
[38] O. C. Zienkiewicz and J. Z. Zhu, A simple error estimator in the finite element method, Int. J. Numer. Methods Engrg., 24 (1987) 337-357.

Appendix A. Projector calculation

Let $\mathcal{P}$ be an linear projector such that

$$\mathcal{P} : \mathcal{V} \to \mathcal{V}^H$$

where $\mathcal{V}$ is a infinite space endowed with an scalar product $(\cdot,\cdot)$ defined on $\mathcal{V}\times\mathcal{V}$, and $\mathcal{V}^H \subset \mathcal{V}$ is a finite dimensional space. The superscript H represents that $\mathcal{V}^H$ is defined on a coarse mesh.

In order to compute numerically $\mathcal{P}$, we also define a fine mesh with a mesh size h associated with the finite space $\mathcal{V}^h \subset \mathcal{V}$. It is supposed the element size of $\mathcal{V}^H$ is much greater than one related to $\mathcal{V}^h$, i.e., $h << H$. Therefore, let $\mathbf{P} : \mathcal{V}^h \to \mathcal{V}^H$ be the projection matrix associated with the projector $\mathcal{P}$.

Let v^H be the basis functions belonging to $\mathcal{V}^H$ and let v^h be the basis functions belonging to $\mathcal{V}^h$. The matricial projector $\mathbf{P}$ can be computed by the following process:

i. The Galerkin-projection of a generic vector $w^h \in \mathcal{V}^h$ into $\mathcal{V}^H$ is given by

$$\int_\Omega \mathcal{L}(w^H)v^H \mathrm{d}\Omega_y = \int_\Omega \mathcal{L}(w^h)v^H \mathrm{d}\Omega_y \qquad \forall v^H \in \mathcal{V}^H \tag{A.1}$$

where $\mathcal{L}$ is the corresponding differential operator. w^H can be expressed as $w^H = \sum_{i=1}^{N} \phi_i^N c_i^N$, where ϕ_i^N are the basis functions of the coarse mesh and c_i^N are the coordinates of w^H for $i = 1, .., N$, being N the degrees of freedom in the coarse mesh. Similarly, w^h can be stated as $w^h = \sum_{j=1}^{n} \phi_j^n c_j^n$, where ϕ_j^n are the basis functions of the coarse mesh and c_j^n are the coordinates of w^h for $j = 1, .., n$, being n the degrees of freedom in the fine mesh.

ii. Eq. (A.1) might be formulated as

$$\boldsymbol{M}^N \boldsymbol{c}^N = \boldsymbol{M}^n \boldsymbol{c}^n \tag{A.2}$$

The matrix $\boldsymbol{M}^N_{(N\times N)}$ is defined as $M^N_{ij} = \int_\Omega \mathcal{L}\phi_i^N \phi_j^N \mathrm{d}\Omega$ for $i, j = 1, ..., N$. Likewise, $\boldsymbol{M}^n_{(N\times n)}$ is established as $M^n_{ij} = \int_\Omega \mathcal{L}\phi_i^n \phi_j^N \mathrm{d}\Omega$ for $i = 1, ..., N$ and $j = 1, ..., n$

iii. Therefore, the coordinates $\boldsymbol{c}^N$ of the vector w^h can be solved as

$$\boldsymbol{c}^N = (\boldsymbol{M}^N)^{-1}\boldsymbol{M}^n \boldsymbol{c}^n \tag{A.3}$$

iv. Finally, the matrix $\mathbf{P}$ associated with the projector $\mathcal{P}$ is

$$\mathbf{P} = (\boldsymbol{M}^N)^{-1}\boldsymbol{M}^n. \tag{A.4}$$

Área de Mecánica de Fluidos, Escuela de Ingeniería y Arquitectura. Universidad de Zaragoza, C/María de Luna 3, 50018 Zaragoza, Spain

E-mail: dirisarri@unizar.es

Área de Mecánica de Fluidos, Escuela de Ingeniería y Arquitectura. Universidad de Zaragoza, C/María de Luna 3, 50018 Zaragoza, Spain

E-mail: gahuke@unziar.es